Journal of Natural Resources and Farming
https://doi.org/10.7770/jonraf-v2-art2908

JONRAF Journal of Natural Resources and Farming

SPECIAL ISSUE

A Conservative Nonlocal Framework for Airborne Fungal Epidemics in Fruit Crops

Marlon M. López-Flores[a*], William Campillay-Llanos[b], Samuel Ortega-Farías[c], Gonzalo A. Díaz[d], Shehzad Iqbal[e,f]

Artificial Intelligence, Robotics and Cybernetics Laboratory, Military Institute of Engineering, Rio de Janeiro[a], Brazil
Núcleo de Investigación en Producción Alimentaria, Facultad de Recursos Naturales, Universidad Católica de Temuco[b], Temuco, Chile
Research and Extension Center for Irrigation and Agroclimatology and Research Program on Adaptation of Agriculture to Climate Change, Universidad de Talca, Talca[c], Chile
Laboratory of Fruit Pathology, Faculty of Agricultural Sciences, Universidad de Talca, Talca[d], Chile
Laboratorio de Investigación Interdisciplinaria en Microbiología Aplicada (LIMA), Facultad de Ciencias de la Salud, Universidad Católica de Temuco, Manuel Montt 56, Campus San Francisco, Temuco[e], Chile
Centro de Investigación, Innovación y Creación (CIIC), Universidad Católica de Temuco, Campus Luis Rivas del Canto, Rudecindo Ortega 03694, Temuco, Región de La Araucanía[f], Chile

Article history
Received: 10/02/2026
Accepted: 15/05/2026
Published: 22/09/2026

Corresponding author
*Marlon M. López-Flores
marlon.michael@ime.eb.br

ABSTRACT

Purpose: Airborne fungal epidemics in fruit crops combine local infection processes with finite-distance inoculum movement; splash-dispersed diseases are considered only as candidate extensions. We developed a conservative nonlocal framework that distinguishes local infection intensity from spatial epidemic footprint and can accommodate polycyclic fruit–pathogen systems after pathogen-specific extension and calibration. **Methods:** Susceptible, latent, and sporulating host tissue were coupled to a nonlocal equation for free inoculum. We establish sufficient conditions for global well-posedness, positivity, and boundedness and derive a spatial next-generation threshold. A synthetic Botrytis cinerea case study used unclipped second-order strong stability-preserving Runge–Kutta [SSPRK(2,2)] simulations to compare local diffusion and nonlocal kernels with moment-matched controls, numerical refinement, periodic and absorbing boundaries, and targeted sensitivity analyses. **Results:** Numerical undershoots remained at roundoff scale. On the 200-m grid, the 5-m Gaussian increased infected-tissue-equivalent length from 30.74 to 33.70 m relative to local diffusion, whereas the original mixed kernel increased it to 88.63 m. With mean and variance matched, changing tail shape increased equivalent length to 39.16 m; an 8-m directional shift increased it to 61.56 m. On a 600-m absorbing domain, broad and directional kernels retained larger footprints than local baselines, although their ranking changed. **Conclusions:** Dispersal scale, tail shape, and directional displacement have distinct effects on epidemic footprint and influence spatial-extent metrics more strongly than peak local infection. The framework is a candidate structure for other fruit diseases, but each application requires pathogen-specific states, forcing, observation models, calibration, and validation.

Keywords: fruit diseases; nonlocal dispersal; fungal epidemiology; spore dispersal kernel; spatial risk; Botrytis cinerea

1. Introduction

Fungal epidemics in fruit crops are driven by interactions among host susceptibility, infection progression, weather, canopy structure, and pathogen dispersal (Madden et al., 2007; Williamson et al., 2007; González-Domínguez et al., 2017; Larena et al., 2022). These processes operate across multiple spatial and temporal scales: local infection depends strongly on tissue condition and microclimate, particularly temperature and moisture, whereas airborne or splash-dispersed inoculum can generate secondary infection foci beyond the immediate neighborhood (Latorre et al., 2012; Ferrada et al., 2015, 2017; Riquelme et al., 2021; Campillay-Llanos et al., 2025). Consequently, plant-disease epidemiology requires models that integrate disease progression with pathogen dispersal (Madden et al., 2007; Brown and Hovmøller, 2002).

A similar broad epidemiological structure occurs in several economically important fruit diseases. *Botrytis cinerea* is a generalist necrotroph that infects flowers, leaves, and fruit in numerous crops and may remain latent before symptoms become visible (Williamson et al., 2007; Elad et al., 2016; Chen et al., 2023). Apple and pear scab caused by *Venturia* species involves primary and secondary inoculum, latent periods, and environmentally regulated infection (González-Domínguez et al., 2017). Brown rot of stone fruit caused by *Monilinia* species also combines inoculum production, dispersal, latent or quiescent infection, and host-stage effects (Holb, 2004; Larena et al., 2022). Anthracnose diseases caused by *Colletotrichum* species affect many temperate and tropical fruits, and conidia can be redistributed by rain splash and under humid conditions (Peres et al., 2020). These systems share epidemiological components that motivate a common candidate state-space structure based on susceptible tissue, latent infection, actively sporulating tissue, and a mobile inoculum pool, although pathogen-specific extensions remain necessary; related compartmental formulations for fruit-disease dynamics have been used previously (Bevacqua et al., 2018; Ortega-Farías et al., 2023).

Most operational disease-warning systems focus on identifying periods when weather and host stage favor infection. Such models are indispensable, but they do not always characterize where inoculum arrives. Conversely, nonlocal dispersal equations represent finite-distance movement through kernels that can accommodate short-range, long-range, or directional transport (Andreu-Vaillo et al., 2010; El Jarroudi et al., 2020). A general framework should connect these two components without counting the same infection twice. In particular, a compartment for latent infection should not be superimposed on an unrelated distributed-delay source unless the relation between the two

descriptions is derived explicitly.

This study develops a conservative nonlocal susceptible–latent–sporulating–inoculum framework for polycyclic fungal diseases of fruit crops. Here, "conservative" refers specifically to the nonlocal transport operator when no boundary loss is imposed; the absorbing-domain variant is sub-conservative because inoculum can leave the modeled domain. *Botrytis cinerea* is used as a case study because its biology provides a clear example of latent infection, active sporulation, broad host range, and airborne conidial movement. The model is formulated as a candidate general framework whose coefficients, environmental response functions, state definitions, and observation equations can be adapted to other pathosystems; transferability beyond the synthetic case study is not claimed to be validated. We hypothesize that dispersal scale, tail shape, and directional displacement have distinct effects on epidemic footprint and that these effects are greater for spatial-extent metrics than for peak local infection. The objectives are to (i) formulate the generic model and its pathogen-specific interpretation, (ii) establish mathematical consistency and a spatial invasion threshold, (iii) evaluate numerical robustness, and (iv) isolate the effects of kernel scale, tail structure, directionality, and boundary assumptions.

2. Materials and Methods

2.1 Generic epidemiological structure

Let $\Omega \subset \mathbb{R}^2$ denote the spatial domain occupied by the crop, such as an orchard, vineyard, greenhouse, or storage facility. A point $x = (x_1, x_2) \in \Omega$ represents a specific location within this domain, whereas $t \geq 0$ denotes time. At each position x and time t, the host is divided into three epidemiological states: susceptible tissue $S(x, t)$, latently infected tissue $E(x, t)$, and sporulating or infectious tissue $I(x, t)$. These variables may represent flowers, leaves, fruits, or other epidemiologically relevant plant tissues. In addition, $u(x, t)$ denotes the local density of free inoculum, such as airborne conidia. From an experimental perspective, $u(x, t)$ can be related to spore-trap measurements collected at different locations within the crop.

The resulting spatial epidemiological model is

$$\begin{cases} \dfrac{\partial S}{\partial t} = -\lambda S u, \\ \dfrac{\partial E}{\partial t} = \lambda S u - \rho E, \\ \dfrac{\partial I}{\partial t} = \rho E - \delta I, \\ \dfrac{\partial u}{\partial t} = \eta \mathcal{L}_J(t) u + \kappa r(x,t) I - m(x,t) u + q(x,t). \end{cases} \tag{1}$$

Infection is mediated by free inoculum: $\lambda S u$ transfers susceptible tissue to the latent class at the same spatial location at which inoculum is present. Latently infected tissue progresses to the sporulating class at rate ρ, and sporulating tissue leaves the actively tracked sporulating class at rate δ. The latter transition is an implicit sink representing loss of active sporulation; a separate recovered or nonsporulating compartment is not modeled. Sporulating tissue produces new inoculum through $\kappa r(x, t)I$, whereas $m(x, t)u$ represents free-inoculum losses due to processes such as mortality, deposition, or wash-off. The term $q(x, t)$ accounts for external or primary inoculum, and $\eta \mathcal{L}_J(t)u$ describes spatial redistribution of inoculum, with η the jump frequency. Thus, the epidemiological cycle represented by system (1) is free inoculum $u \to E \to I \to u$. No direct $S \to E$ transmission from sporulating host tissue is included; all new infections are mediated through the free-inoculum compartment.

When $u \equiv 0$ and $q \equiv 0$, no new infections occur and the host subsystem reduces to progression of any initially infected tissue,

$$\begin{cases} \dfrac{dS}{dt} = 0, \\ \dfrac{dE}{dt} = -\rho E, \\ \dfrac{dI}{dt} = \rho E - \delta I. \end{cases} \tag{2}$$

This host-progression subsystem is shown only to clarify the compartmental transitions used in the spatial model; the numerical experiments below solve the full system (1).

Figure 1.
Schematic representation of the host-progression component of the model. Free inoculum causes susceptible tissue (S) to enter the latent class (E) at rate $\lambda S u$. Latently infected tissue progresses to the sporulating class (I) at rate ρE, and sporulating tissue leaves the actively tracked class at rate δI. The free-inoculum compartment is omitted here for visual simplicity and is shown in Fig. 2.

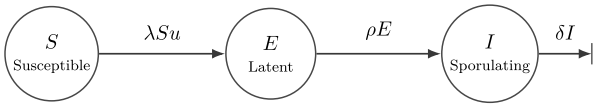

The nonlocal dispersal operator depends on the boundary treatment. For a conservative kernel on Ω, define

$$\mathcal{L}_J^{\mathrm{c}} u(x) = \int_\Omega J(x, y, t) u(y)\, dy - u(x) \int_\Omega J(y, x, t)\, dy. \tag{3}$$

Here $J(x, y, t)$ describes inoculum movement from y to x, and direct integration shows that $\int_\Omega \mathcal{L}_J^{\mathrm{c}} u dx = 0$. For a translation-invariant, normalized periodic kernel $J(x, y) = K(x - y)$, this becomes $\mathcal{L}_K^{\mathrm{per}} u = K_{*\mathrm{per}}\, u - u$.

For the absorbing-domain experiment, the model uses zero extension outside Ω. If $K \geq 0$ is normalized on the full space, the corresponding operator is

$$\mathcal{L}_K^{\mathrm{abs}} u(x) = \int_\Omega K(x - y) u(y)\, dy - u(x). \tag{4}$$

In this case $\int_\Omega \mathcal{L}_K^{\mathrm{abs}} u dx \leq 0$, with strict loss whenever dispersal carries mass outside the domain. Equations (3) and (4) therefore distinguish conservative periodic transport from absorbing boundary loss without changing the within-domain infection dynamics (Du et al., 2012; D'Elia et al., 2020). In (1), $\mathcal{L}_J$ denotes the operator appropriate to the stated boundary condition.

Figure 2.

Schematic representation of the full spatial epidemiological model. Free inoculum $u(x, t)$ generates latent infections at rate λSu. Latent tissue progresses to sporulation at rate ρE, sporulating tissue produces inoculum at rate $\kappa r(x, t)I$, and free inoculum is lost at rate $m(x, t)u$. External inoculum enters through $q(x, t)$, while $\eta\mathcal{L}_J(t)u$ represents spatial redistribution under the selected boundary treatment. In practice, $u(x, t)$ can be informed by or calibrated against spore-trap or airborne-propagule measurements collected at different locations and times, including molecular and automated real-time monitoring technologies developed for airborne plant pathogens (Muthukumar et al., 2025; Malvessi Cattani et al., 2026).

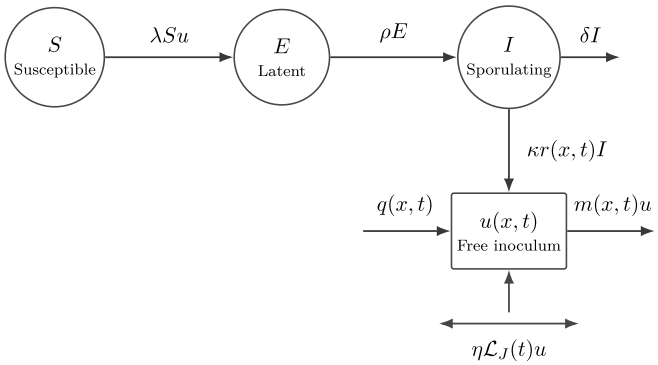

2.2 Velocity-jump interpretation

A dispersal kernel can be derived from a transport–turning–deposition process (Othmer et al., 1988; El Jarroudi et al., 2020). Let $p(z, v, t \mid v_0)$ denote the subprobability density of a spore that remains airborne at displacement z and velocity v, conditional on initial velocity v_0. With turning rate γ, post-turning velocity distribution qv, and deposition hazard μ,

$$\partial_t p + v \cdot \nabla_z p = -(\gamma + \mu)p + \gamma q_V(v) \int_V p(z, w, t \mid v_0)\, dw. \quad (5)$$

The deposition displacement density is

$$K(z) = \mu \int_0^\infty \int_V \int_V p(z, v, t \mid v_0)\, \pi(dv_0)\, dv\, dt. \quad (6)$$

Because p already includes survival against deposition, no additional survival factor is required. If eventual deposition occurs with probability one, then $\int K(z)\mathrm{d}z = 1$.

2.3 Potential pathosystem transfer

The model is not intended to imply identical biology across fruit pathogens. The case study represents an airborne, *B.* cinerea-like system; splash-dispersed diseases are considered only as candidate extensions. The framework provides a state-space structure whose states, coefficients, forcing functions, and observation models must be revised for each disease. Tables I and II summarize biologically compatible interpretations and required extensions; they neither demonstrate transferability nor provide validated parameterizations.

2.4 Well-posedness, positivity, and boundedness

We use the following sufficient assumptions: (A1) Ω is compact; (A2) $J(\cdot, \cdot, t)$ and all coefficients are bounded and nonnegative, with ρ and δ interpreted as transition rates; (A3)

Table 1

Compatible state interpretations for selected fungal diseases of fruit crops. These correspondences are conceptual and are not validated pathogen-specific models.

Pathosystem	*S*	*E*	*I*	*u*
B. cinerea gray mold (Williamson et al., 2007; Chen et al., 2023)	flowers, leaves, or fruit	latent/quiescent infection	sporulating lesions	airborne conidia
Venturia spp. scab (González-Domínguez et al., 2017)	leaves and fruit	latent lesions	conidial lesions	ascospores/conidia
Monilinia spp. brown rot (Holb, 2004; Larena et al., 2022)	blossoms or fruit	latent infection	sporulating rot	lesion/mummy conidia
Colletotrichum spp. anthracnose (Peres et al., 2020)	fruit or tissue	quiescent infection	acervuli-bearing tissue	splash-dispersed conidia

Table II

Pathogen-specific extensions required before applying the candidate framework.

Pathosystem	Source structure	Forcing	Observations/additional states
B. cinerea	external and lesion-derived conidia	wetness, temperature, organ, phenology	spore traps, latent assays, organ classes
Venturia spp.	primary ascospores and secondary conidia	leaf emergence, ascospore maturity, temperature, wetness	separate inoculum classes; lesion maturation
Monilinia spp.	blossom, fruit, and mummified-fruit sources	host stage, wounding, harvest, storage	blossom/fruit classes; postharvest transitions
Colletotrichum spp.	rain-splash conidia	wetness, rain, fruit maturity, species complex	quiescent infection; postharvest activation

$t \mapsto \eta\mathcal{L}_J$ is strongly measurable and locally bounded on $C(\Omega)$ and generates a positive contraction evolution family for the selected periodic or absorbing boundary treatment; and (A4) the reaction terms are locally Lipschitz on $X = C(\Omega)$[4].

Proposition 1 (Global well-posedness) *Under assumptions A1–A4, nonnegative initial data generate a unique global nonnegative mild solution. If, in addition, $m \geq m_\star > 0$, $\kappa r \leq b^\star$, and $q \leq q^\star$, then the solution is uniformly bounded for all $t \geq 0$.*

Proof sketch. Standard semigroup and evolution-equation theory in Banach spaces yields a unique local mild solution (Pazy, 1983). Quasipositivity of the reaction terms and positivity of the evolution family associated with $\eta\mathcal{L}_J(t)$ imply forward invariance of X_+. Because the dispersal evolution family is positive and contractive and $m(x, t) \geq m_\star > 0$, the variation-of-constants formula permits comparison of the inoculum component with the scalar equation $v' = -m_\star v + b\|N_0\|_\infty + q^\star$ in the L^∞ norm. Summing the first three equations of (1), the tracked host-tissue total $N = S + E + I$ satisfies

$$\partial_t N = -\delta I \leq 0, \tag{7}$$

so $0 \leq S, E, I \leq \|N(\cdot, 0)\|_\infty$. Moreover,

$$\|u(t)\|_\infty \leq e^{-m_* t}\|u_0\|_\infty + \int_0^t e^{-m_*(t-s)}\,(b^*\|N_0\|_\infty + q^*)\; ds. \tag{8}$$

Evaluating the integral gives

$$\|u(t)\|_\infty \leq \|u_0\|_\infty + \frac{b^*\|N_0\|_\infty + q^*}{m_*}, \qquad t \geq 0. \tag{9}$$

Thus the full state is uniformly bounded for all $t \geq 0$, finite-time blow-up is excluded, and the local solution extends globally.

2.5 Spatial invasion threshold

Following the next-generation-operator approach for heterogeneous epidemic systems (Diekmann et al., 1990; van den Driessche and Watmough, 2002), we define a spatial invasion threshold for the linearized infection cycle. For autonomous coefficients, assume $q = 0$, $m(x) \geq m_\star > 0$, $\rho(x) \geq \rho_\star > 0$, $\delta(x) \geq \delta_\star > 0$, and continuous multiplication coefficients. Let $A = M_m - \eta\mathcal{L}_J$ on $C(\Omega)$, where $\mathcal{L}_J$ is either the periodic conservative operator or the absorbing zero-extension operator defined above, and assume that $\mathcal{L}_J$ is bounded and generates a positive contraction semigroup.

Proposition 2 (Spatial next-generation threshold). *The operator -A generates a positive exponentially stable semigroup, A^{-1} exists and is positive, and the next-generation operator on $C(\Omega)$ is*

$$\mathcal{K} = M_{\lambda S_0} A^{-1} M_{\kappa r/\delta}, \qquad R_0 = r(\mathcal{K}). \tag{10}$$

For homogeneous coefficients and a normalized periodic kernel, $R_0 = \lambda S_0 \kappa r/(m\delta)$.

Justification. Exponential stability gives

$$A^{-1} = \int_0^\infty e^{-tA}\, dt, \tag{11}$$

which is positive. The infection cycle is $E \to I \to u \to E$. Because progression at rate ρ is the only exit from E, one unit of latent tissue reaches I with probability one. At a fixed location, a unit of sporulating tissue remains in I for mean time $1/\delta$ and therefore produces $\kappa r/\delta$ inoculum units in expectation. The positive resolvent A^{-1} accounts for inoculum residence and spatial redistribution before loss, and multiplication by λS_0 converts free inoculum into new latent infections. We define the invasion threshold through the spectral radius of this positive operator. Existence of a principal eigenfunction requires additional compactness or irreducibility assumptions (Shen and Xie, 2015) and is not needed for the threshold definition used here. The rate ρ affects generation timing but not expected offspring under the stated assumption that progression is the sole exit from E.

2.6 Case study and numerical experiments

The numerical study represents a one-dimensional specialization of (1) for a generic orchard row under a *B. cinerea*-like parameter regime. The parameters are synthetic and are intended to isolate transport mechanisms rather than predict outcomes for a specific crop. In the simulations, S, E, and I are tissue fractions and u is a dimensionless scaled inoculum density; accordingly, the infection and inoculum-production coefficients are interpreted on this scaled state space. The production experiment used a 200-m-long periodic transect with $N = 256$ points and $\Delta t = 0.0025$ day. Initial conditions were $S(x, 0) = 1$, $E(x, 0) = I(x, 0) = 0$, and

$$u(x, 0) = 0.08 \exp\left[-\frac{d_{\mathrm{per}}(x, 50)^2}{2(2\ \mathrm{m})^2}\right]. \tag{12}$$

All numerical experiments set $q \equiv 0$, so the prescribed initial inoculum is the only external seeding of the simulated epidemic. The parameters were $\lambda = 0.50$, $\rho = 1/3$, $\delta = 0.20$, $\kappa r = 3.0$, $m = 1.0$, and $\eta = 0.9$ day^{-1}. Nonlocal kernels were normalized on the discrete grid and convolved using the fast Fourier transform; the refinement study followed the principle that spatial and temporal discretization errors should be examined separately in nonlocal approximations (Tian and Du, 2013). The local baseline solved $\partial_t u = D_{\mathrm{loc}}\partial_{xx} u + \kappa r I - m u$, with $D_{\mathrm{loc}} = \eta\sigma_K^2/2 = 11.25\mathrm{m}^2\mathrm{day}^{-1}$, where $\sigma_K = 5$ m is the standard deviation of the moment-matched Gaussian kernel.

Time integration used the unclipped second-order strong stability-preserving Runge–Kutta [SSPRK(2,2)] method (Gottlieb et al., 2001). Spatial refinement varied $N = 128, 256, 512$ at fixed $\Delta t = 0.0025$ day. Temporal refinement used $\Delta t = 0.01, 0.005, 0.0025$ day at fixed $N = 256$. The primary metrics were affected length, infected-tissue-equivalent length $\int_\Omega (E + I)\mathrm{d}x$, peak local infection, spatial spread, centroid, and times to 50%, 75%, and 90% coverage. Periodic simulations used a circular centroid and circular spread; absorbing-domain simulations used ordinary first and second spatial moments.

Three controlled blocks were used to separate the mechanisms: (A) centered Gaussian kernels with standard deviations 5, 10, and 20 m; (B) a 5-m Gaussian and a two-component Gaussian mixture with the same mean and

variance but greater fourth central moment; and (C) 5-m Gaussian kernels shifted by 0, 4, and 8 m. Boundary robustness was assessed on a 600-m domain with absorbing boundaries for both the nonlocal and local-diffusion models. Targeted one-factor sensitivity analyses varied λ, η, and the initial inoculum amplitude. These analyses were interpreted as structural robustness checks rather than calibrated response surfaces. The computational package contains the generation script, a fixed software environment, machine-readable outputs, an immutable checksum manifest, and an independent validation script.

3 Results

3.1 Numerical verification

The unclipped solver remained nonnegative within numerical precision. On the 200-m production runs, the largest undershoot was 1.7×10^{-19} and the accumulated negative magnitude was negligible relative to state values of order 10^{-1}. Nonlocal scenarios changed by less than 0.001% between $N = 256$ and $N = 512$. The local-diffusion baseline changed from 30.7445 to 30.7229 m in infected-tissue-equivalent length, a 0.070% difference. The separate temporal-refinement analysis produced smaller changes than the spatial-refinement analysis at $N = 256$. These results support numerical robustness for the reported settings, although they do not constitute a general convergence theorem.

3.2 Primary comparison

Fig. 3 shows the normalized kernels. On the production grid, local diffusion affected 130.47 m and yielded an infected-tissue-equivalent length of 30.74 m. The moment-matched 5-m Gaussian affected 146.09 m and yielded an equivalent length of 33.70 m, increases of approximately 12% and 10%, respectively. The 20-m Gaussian, original mixture, and wind-shifted kernel reached the full 200-m periodic transect. Their 90% coverage times were 10.25, 12.50, and 16.25 days, whereas the 5-m Gaussian and local diffusion did not reach 90% coverage by day 30.

The original mixture produced an equivalent length approximately 188% greater than that produced by local diffusion, while its peak fraction was slightly lower. This comparison quantifies the combined effect of scale and tail structure; it does not isolate tail shape because the original kernels are not matched in all moments. Fig. 4 confirms that similar local peaks can coexist with markedly different spatial footprints.

3.3 Controlled mechanism comparisons

The controlled comparisons separated the effects of scale, tail shape, and directional displacement (Fig. 5). Increasing Gaussian scale from 5 to 20 m increased equivalent length from 33.70 to 85.13 m. At equal mean and variance, the heavier-tailed matched mixture increased equivalent length from 33.70 to 39.16 m and affected length from 146.09 to approximately 177 m, while slightly reducing peak infection. Shifting the same 5-m Gaussian by 8 m increased equivalent length to 61.56 m and displaced the epidemic centroid. Thus, scale, higher-order kernel shape, and mean displacement produced distinct responses.

3.4 Boundary robustness

The separation in epidemic footprint was not restricted to the periodic 200-m setting. On a 600-m-long absorbing domain, local diffusion and the 5-m Gaussian produced equivalent lengths of 30.44 and 33.07 m, respectively, whereas the original mixture, 20-m Gaussian, and wind-shifted kernel produced 69.34, 82.47, and 83.23 m. Inoculum leaving the domain was removed rather than wrapped to the opposite boundary. Absorbing boundaries therefore preserved the substantially larger footprints associated with broad and directional transport relative to the local and short-range baselines, but altered the ranking among the three broad or directional kernels (Fig. 6). The integrated nonlocal boundary-loss diagnostic is provided in the machine-readable output.

3.5 Epidemiological sensitivity

Sensitivity analyses showed that the broad-kernel footprint remained distinct across the tested infection efficiencies, jump frequencies, and initial inoculum amplitudes (Fig. 7). The responses were not uniformly monotonic. Diagnostic state integrals and peak times indicate that parameter changes can advance epidemic timing and alter susceptible-tissue depletion and spatial redistribution; these mechanisms may reduce the day-30 integral even when early spread is more rapid. The sensitivity results are therefore structural robustness checks rather than calibrated response surfaces or simple causal laws.

Table VI documents the nonmonotone response to infection efficiency. At $\lambda = 0.65$, infection peaked earlier and susceptible tissue was almost exhausted by day 30, so the day-30 equivalent length was lower than at the nominal value despite faster early spread. These diagnostics support the proposed timing-and-depletion interpretation without implying a general causal law.

4. Discussion

The principal finding is that local epidemic severity and spatial epidemic footprint are not interchangeable observables. Kernels that produce similar local peaks can generate very different affected lengths, spatial spreads, and coverage times. This distinction is important for disease monitoring: calibration based only on disease severity at a small number of sites may identify infection efficiency but fail to resolve dispersal scale, tail structure, or directionality. Spatially distributed spore traps and disease assessments are therefore needed when transport parameters are of interest.

The state-space structure is potentially transferable beyond *B. cinerea*, but transfer has not yet been demonstrated through pathogen-specific calibration or validation. For *Venturia* spp., the framework could separate ascospore or conidial arrival from local infection and lesion maturation, but primary and secondary inoculum should be modeled separately. For *Monilinia* spp., blossom blight, fruit infection,

Table III

Synthetic baseline parameters and numerical settings for the *B.* cinerea-like case study. Values are mechanism-isolating inputs rather than estimates for a specific crop or site.

Quantity	Interpretation	Baseline value	Sensitivity values
λ	scaled infection coefficient	0.50 day^{-1}	0.35, 0.50, 0.65 day^{-1}
ρ	latent-to-sporulating rate	1/3 day^{-1}	not varied
δ	loss of sporulation	0.20 day^{-1}	not varied
κr	scaled inoculum production	3.0 day^{-1}	not varied
m	free-inoculum loss	1.0 day^{-1}	not varied
η	jump frequency	0.9 day^{-1}	0.6, 0.9, 1.2
A_0	scaled initial inoculum amplitude	0.08	0.04, 0.08, 0.12
$L,N,\Delta t$	production domain, grid, step	200 m, 256, 0.0025 day	refinement described in text

Table IV

Summary of numerical refinement and positivity diagnostics. Spatial error compares $N = 256$ and $N = 512$ at $\Delta t = 0.0025$ day; temporal error compares $\Delta t = 0.005$ and 0.0025 day at $N = 256$.

Model	Spatial change (%)	Temporal change (%)	Minimum state
Gaussian 5 m	< 0.001	< 0.001	-6.7×10^{-19}
Gaussian 20 m	< 0.001	< 0.001	0
Original mixture	< 0.001	< 0.001	0
Wind-shifted	< 0.001	< 0.001	-3.8×10^{-24}
Local diffusion	0.070	< 0.001	0

Table V

Primary day-30 metrics on the 200-m production grid. Equivalent length is $\int(E + I)dx$. A dash indicates that the stated coverage level was not reached by day 30.

Transport	Affected (m)	Equivalent length (m)	Peak fraction	t50 (d)	t75 (d)	t90 (d)
Local diffusion	130.47	30.74	0.557	22.75	–	–
Gaussian 5 m	146.09	33.70	0.553	20.00	–	–
Gaussian 20 m	200.00	85.13	0.564	6.00	8.75	10.25
Original mixture	200.00	88.63	0.552	7.25	11.00	12.50
Wind-shifted	200.00	79.57	0.586	8.75	13.50	16.25

Table VI

Diagnostics for the one-factor sensitivity analysis in infection efficiency λ. State integrals are evaluated at day 30 on the 200-m periodic domain.

λ	Equivalent length (m)	Peak time (d)	$\int S\,dx$	$\int E\,dx$	$\int I\,dx$
0.35	51.96	30.0	117.80	25.59	26.37
0.50	88.63	29.0	23.99	34.60	54.03
0.65	65.47	24.5	1.29	15.76	49.70

Figure 3.

Normalized periodic dispersal kernels used in the primary comparison. Line styles and markers permit interpretation without relying on color. Discrete mass, mean, variance, fourth central moment, and kurtosis are reported in the computational archive.

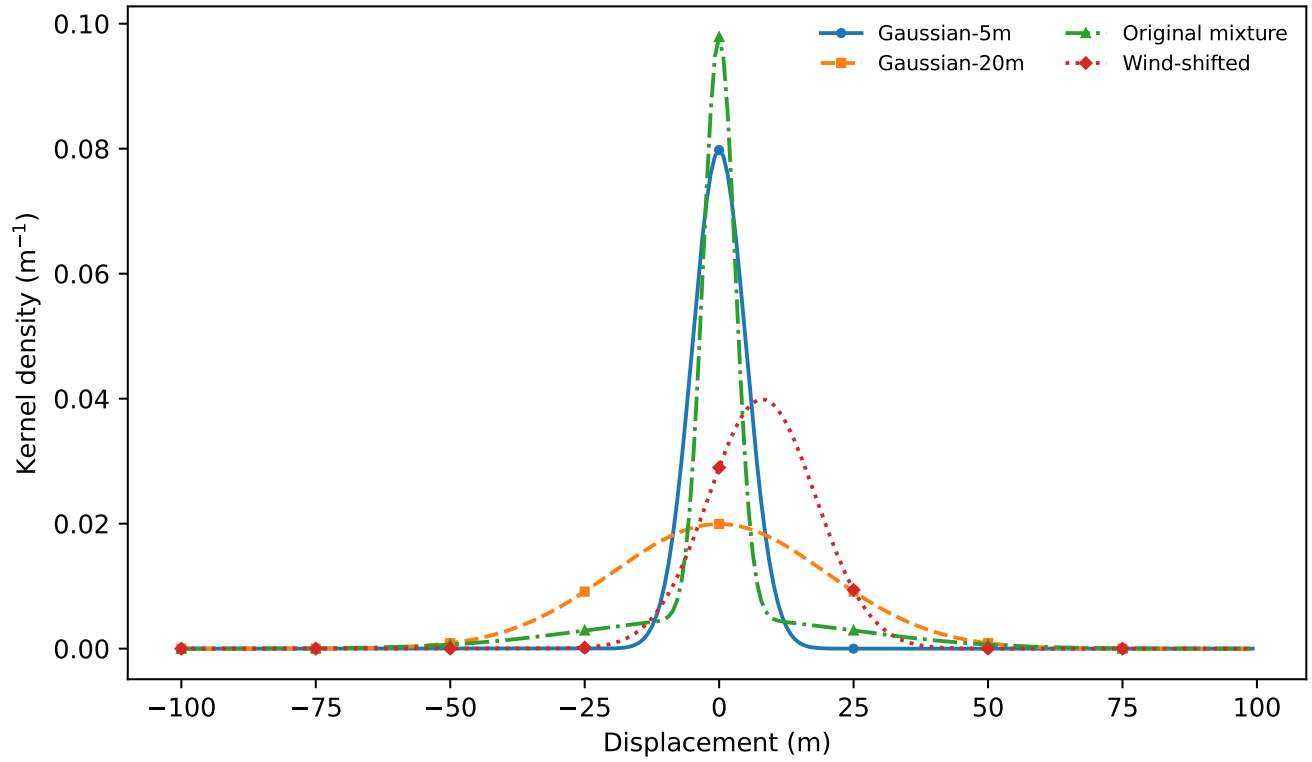

Figure 4.

Latent plus sporulating tissue at day 30 on the 200-m periodic orchard-row transect. The vertical line marks the initial inoculum center; affected length used the threshold $E + I > 10^{-3}$.

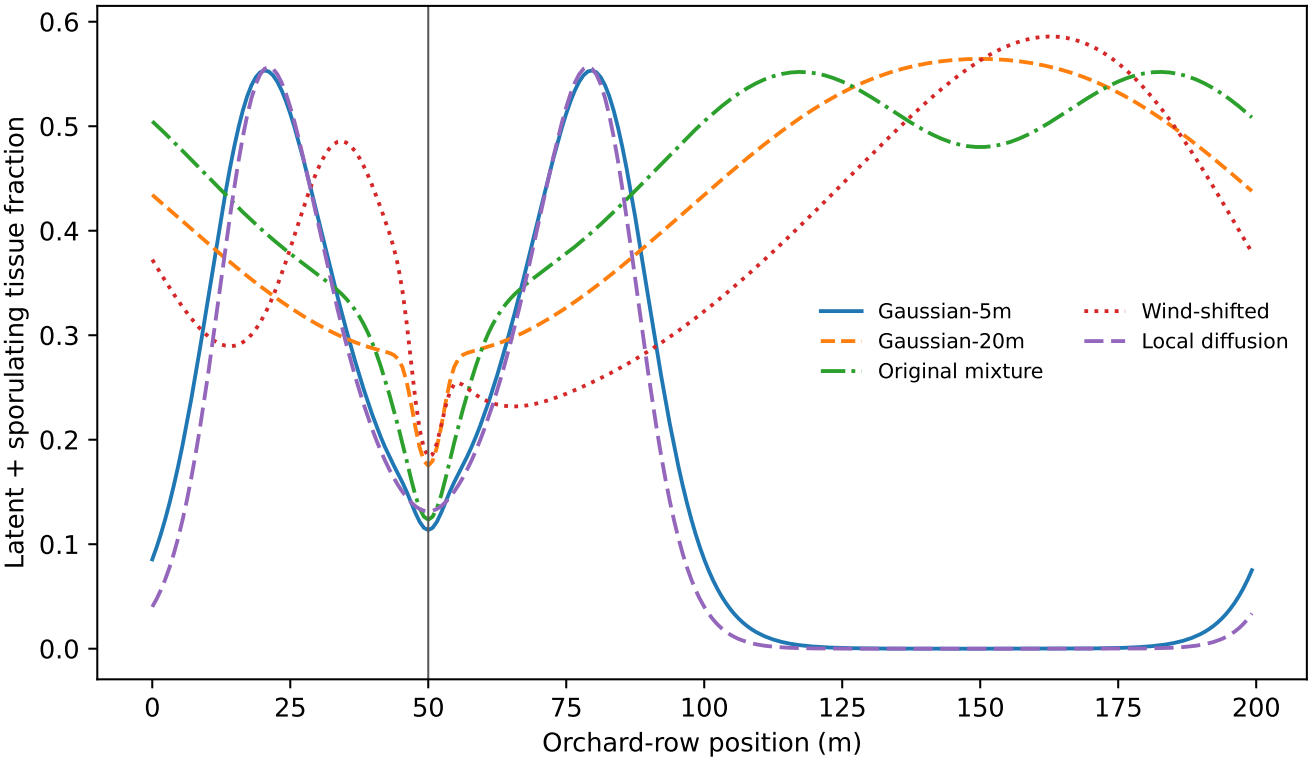

Figure 5.

Controlled comparisons that separate dispersal scale, tail shape at matched variance, and directional displacement. The upper row shows infected-tissue-equivalent length on common limits; the lower row shows peak local infection.

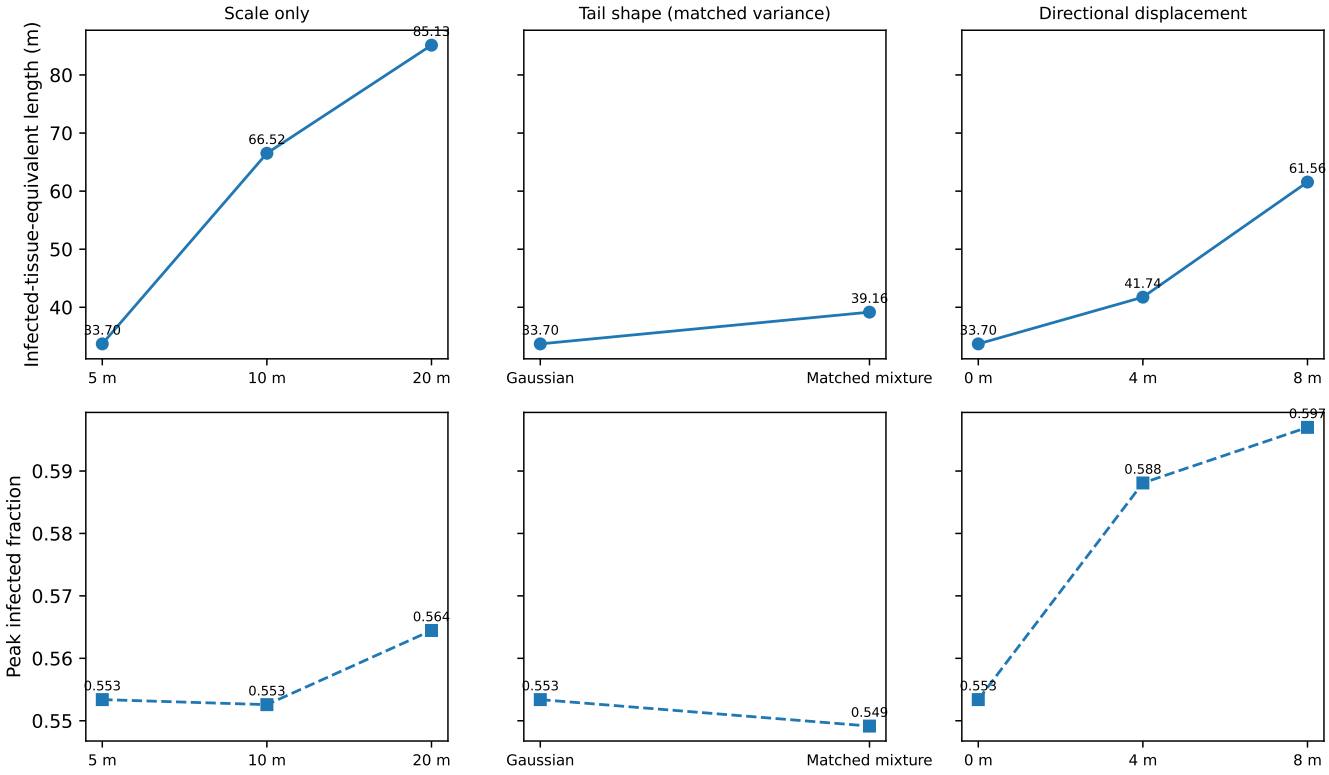

Figure 6.

Day-30 infected-tissue-equivalent length and peak infection on a 600-m absorbing domain.

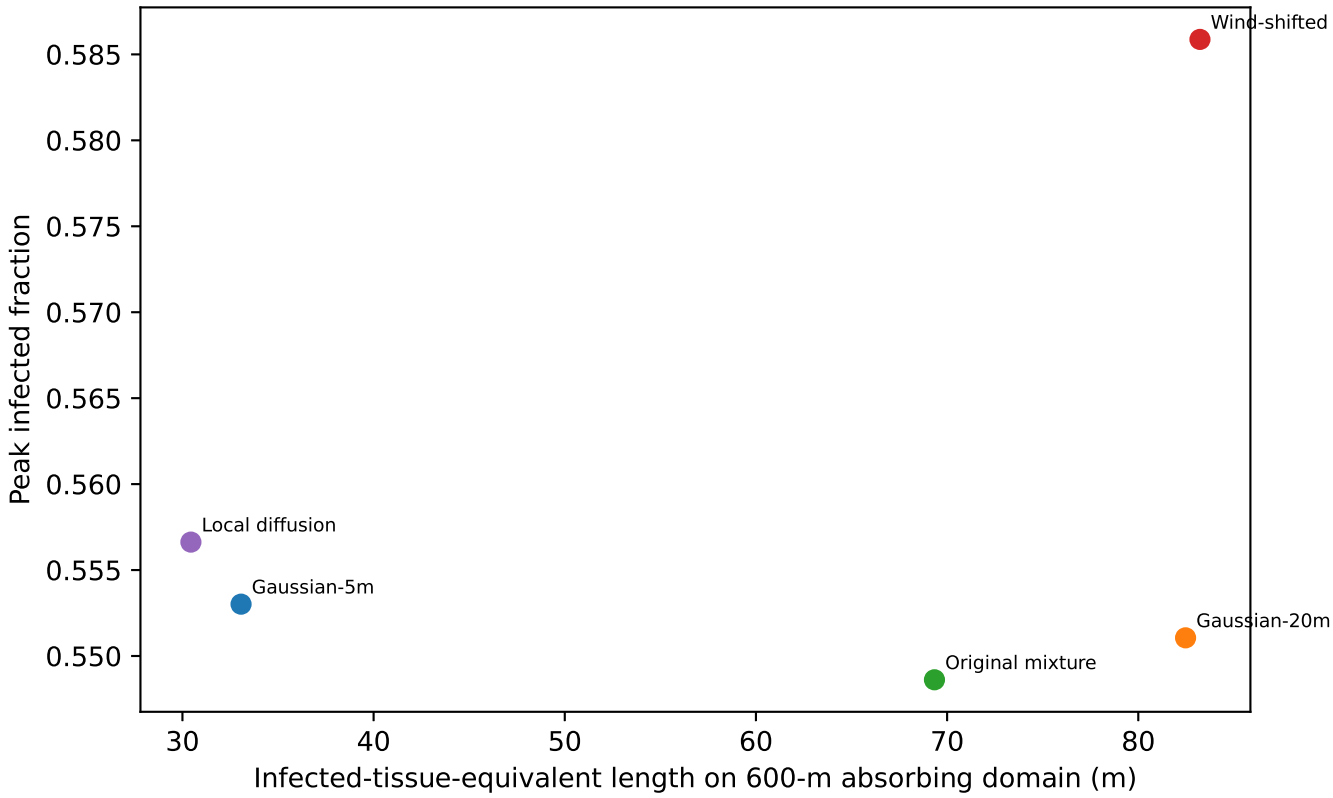

Figure 7.

One-factor sensitivity of the original mixed-kernel scenario to infection efficiency λ, jump frequency η, and initial inoculum amplitude. Labels show day-30 infected-tissue-equivalent length.

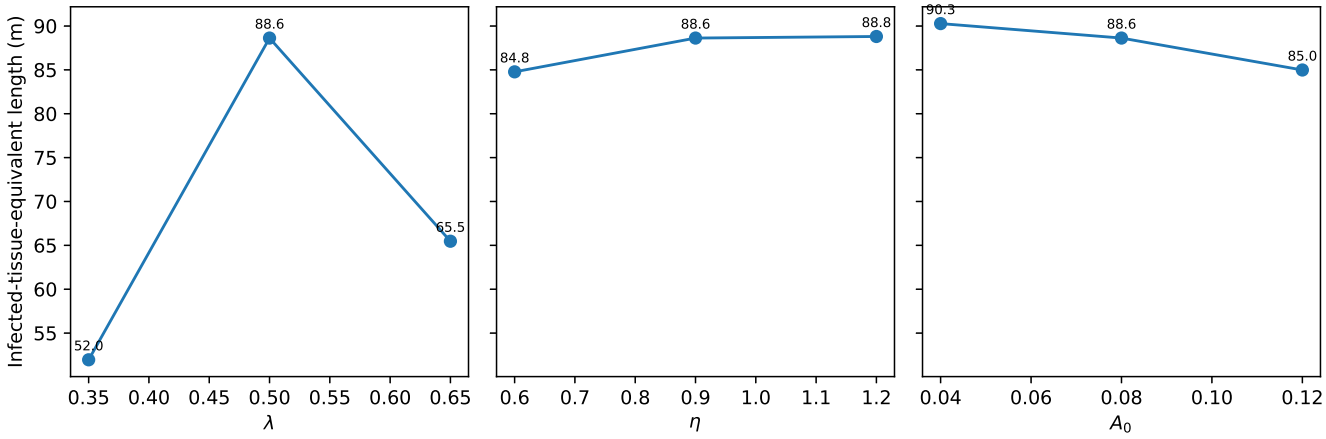

mummified-fruit sources, and postharvest transitions may require multiple tissue classes. For *Colletotrichum* spp., rain-splash kernels and quiescent fruit infection are likely more important than a purely airborne kernel. These examples identify plausible extensions of the candidate structure rather than demonstrating transferability of the model equations or numerical parameters.

The present formulation deliberately excludes a separate direct $S \to E$ transmission term driven by sporulating tissue. This choice makes the free-inoculum compartment the unique infection pathway and avoids double counting transmission that is already represented through inoculum production and dispersal. If pathogen-specific evidence supports an additional contact- or proximity-mediated route, that mechanism could be reintroduced as an explicit extension and would require a corresponding re-derivation of the invasion threshold.

The mathematical threshold provides a spatial analogue of a reproduction number. It decomposes epidemic invasion into infection efficiency, lesion productivity, inoculum loss, and spatial residence. In heterogeneous orchards, R_0 is the spectral radius of an operator rather than a single local product. This formulation shows that identical local biological parameters can yield different invasion potentials when transport and loss vary spatially.

The controlled comparisons clarify the role of kernel moments. Increasing the Gaussian scale produced the largest change in the present experiments. At fixed mean and variance, greater tail weight also increased the footprint, but its effect was smaller than that of the scale contrast. Directional displacement changed both total footprint and epidemic location. These distinctions would be obscured if only an unmatched broad mixture were compared with local diffusion.

The boundary analysis is relevant to orchard applications. Periodic domains are useful for controlled mechanism studies, but they recycle inoculum across boundaries. The absorbing-domain experiment removed periodic recirculation and preserved the separation between broad or directional transport and the local or short-range baselines, although the internal ranking among broad kernels changed. Real orchards may require partially absorbing, reflective, advective, or landscape-coupled boundaries, depending on surrounding vegetation and wind.

The sensitivity diagnostics help explain the observed nonmonotonicity, but they are limited to one-factor analyses and do not quantify parameter interactions. The study has limitations. The parameters are synthetic and are not estimates for any specific crop or production system. Host tissue is aggregated into a single class, environmental forcing is held constant, and structural identifiability has not been established. The model does not represent fungicide decay, cultivar resistance, canopy architecture, rain events, or postharvest handling. The *B. cinerea* example is therefore mechanistic and hypothesis-generating. Application to fruit-production systems requires pathogen-specific observation equations, parameter estimation from spore counts and disease assessments, uncertainty quantification, and independent validation across sites or seasons.

5. Conclusions

A conservative nonlocal susceptible–latent–sporulating–inoculum model provides a candidate representation of fungal epidemics in fruit crops when infection occurs locally but inoculum moves over finite distances. The analysis establishes positivity, boundedness, and a spatial invasion threshold under explicit operator assumptions. In the synthetic *B. cinerea* case study, dispersal scale, tail shape, and directional displacement changed epidemic footprint more strongly than peak local infection. This conclusion was supported by moment-matched controls, separate spatial and temporal refinement analyses, and an absorbing-boundary test; however, the ranking among broad and directional kernels depended on the boundary treatment. The framework provides a candidate structure for scab, brown rot, anthracnose, and related diseases, but each application requires pathogen-specific extensions, observation models, calibration, uncertainty analysis, and

independent validation before it can support operational risk mapping or management recommendations.

Declarations

Competing interests. The authors declare no competing interests.

Funding. M.M.L.-F. received partial funding from project EVAAT-GCN under FINEP agreement 01.24.0661.00, ref. 3311/24.

Author contributions. The definitive CRediT statement is provided in the separate title-page file.

Data and code availability. No empirical data were analyzed. The code, machine-readable simulation outputs, software-environment specification, checksum manifest, and validation files used to generate the numerical results are provided as supplementary material and are also available from the corresponding author upon reasonable request.

Ethics approval and consent. Not applicable.

Acknowledgments. The authors thank their institutions for academic support during the preparation of this manuscript.

Use of artificial intelligence. A language model was used to assist with editorial drafting, LaTeX and Word document preparation, and code development. It was not listed as an author. The human authors independently verified the data processing, equations, implementation, numerical outputs, references, interpretations, and conclusions.

References

Andreu-Vaillo F, Mazón JM, Rossi JD, Toledo-Melero JJ (2010) *Nonlocal Diffusion Problems*. American Mathematical Society, Providence. https://doi.org/10.1090/surv/165

Bevacqua D, Quilot-Turion B, Bolzoni L (2018) A model for temporal dynamics of brown rot spreading in fruit orchards. *Phytopathology* 108(5):595–601. https://doi.org/10.1094/PHYTO-07-17-0250-R

Brown JKM, Hovmøller MS (2002) Aerial dispersal of pathogens on the global and continental scales and its impact on plant disease. *Science* 297:537–541. https://doi.org/10.1126/science.1072678

Campillay-Llanos W, Ortega-Farías S, González-Colville P, Díaz GA, López-Flores MM, López-Olivari R (2025) Modeling the effects of extreme temperatures on the infection rate of *Botrytis cinerea* using historical climate data (1951–2023) of Central Chile. *Agronomy* 15(3):608. https://doi.org/10.3390/agronomy15030608

Chen T, Nomura K, Wang X, Sohrabi R, Xu J, Yao L, Paasch BC, Ma L, Kremer J, Cheng Y, Zhang L, Wang N, Wang E, Xin XF, He SY (2023) *Botrytis cinerea*. *Curr Biol* 33:R187–R188. https://doi.org/10.1016/j.cub.2023.01.034

D'Elia M, Tian X, Yu Y (2020) A physically consistent, flexible, and efficient strategy to convert local boundary conditions into nonlocal volume constraints. *SIAM J Sci Comput* 42:A1935–A1949. https://doi.org/10.1137/19M1266617

Diekmann O, Heesterbeek JAP, Metz JAJ (1990) On the definition and computation of the basic reproduction ratio in heterogeneous populations. *J Math Biol* 28:365–382. https://doi.org/10.1007/BF00178324

Du Q, Gunzburger M, Lehoucq RB, Zhou K (2012) Analysis and approximation of nonlocal diffusion problems with volume constraints. *SIAM Rev* 54:667–696. https://doi.org/10.1137/110833294

Elad Y, Pertot I, Cotes Prado AM, Stewart A (2016) Plant hosts of *Botrytis* spp. In: Fillinger S, Elad Y (eds) *Botrytis – the Fungus, the Pathogen and its Management in Agricultural Systems*. Springer, Cham, pp 413–486. https://doi.org/10.1007/978-3-319-23371-0_20

El Jarroudi M, Karjoun H, Kouadio L, El Jarroudi M (2020) Mathematical modelling of non-local spore dispersion of wind-borne pathogens causing fungal diseases. *Appl Math Comput* 376:125107. https://doi.org/10.1016/j.amc.2020.125107

Ferrada EE, Zoffoli JP, Díaz GA, Latorre BA (2015) First report of *Botrytis cinerea* causing blossom blight on Japanese plums in Chile. *Plant Dis* 99(6):888. https://doi.org/10.1094/PDIS-11-14-1110-PDN

Ferrada EE, Lolas M, Pacheco C, Díaz GA (2017) Occurrence of severe outbreak of calyx-end rot associated with *Botrytis cinerea* in *Malus domestica* cv. Cripps Pink during harvest in the Maule Region, Chile. *Plant Dis* 101(12):2149. https://doi.org/10.1094/PDIS-05-17-0636-PDN

González-Domínguez E, Armengol J, Rossi V (2017) Biology and epidemiology of *Venturia* species affecting fruit crops: a review. *Front Plant Sci* 8:1496. https://doi.org/10.3389/fpls.2017.01496

Gottlieb S, Shu C-W, Tadmor E (2001) Strong stability-preserving high-order time discretization methods. *SIAM Rev* 43:89–112. https://doi.org/10.1137/S003614450036757X

Holb IJ (2004) The brown rot fungi of fruit crops (*Monilinia* spp.): II. Important features of their epidemiology. *Int J Hortic Sci* 10:17–33. https://doi.org/10.31421/IJHS/10/1/435

Larena I, Villarino M, Melgarejo P, De Cal A (2022) Brown rot on stone fruit: from epidemiology studies to the development of effective control strategies. *Sci Hortic* 303:111096. https://doi.org/10.1016/j.scienta.2022.111096

Latorre BA, Rojas S, Díaz GA, Chuaqui H (2012) Germicidal effect of UV light on epiphytic fungi isolated from blueberry. *Cien Inv Agr* 39(3):473–480. https://doi.org/10.4067/S0718-16202012000300007

Malvessi Cattani A, Zeder Y, Graf E, Schwendimann A, Coronelli R, Smit-Sadki T, et al. (2026) Automated air-flow cytometry enables real-time monitoring of *Plasmopara viticola* sporangia in vineyards. *Appl Environ Microbiol* 92(4):e02152-25. https://doi.org/10.1128/aem.02152-25

Madden LV, Hughes G, van den Bosch F (2007) *The Study of Plant Disease Epidemics*. APS Press, St. Paul. https://doi.org/10.1094/9780890545058

Muthukumar G, Kamalakannan A, Johnson I, Kamaraj P, Muthuvel I, Varanavasiappan S, Angayarkanni T (2025) Early detection and quantification of airborne inocula of *Plasmopara viticola* causing grapevine downy mildew using an impaction spore trap. *Physiol Mol Plant Pathol* 139:102842. https://doi.org/10.1016/j.pmpp.2025.102842

Ortega-Farías S, Díaz GA, Campillay-Llanos W, López-Flores MM (2023) Digitalized biomathematical models for the dynamic analysis of gray mold caused by *Botrytis cinerea* in wine grapes: Insights and applications. *2023 IEEE CHILEAN Conference on Electrical, Electronics Engineering, Information and Communication Technologies (CHILECON)*, pp 1–6. IEEE. https://doi.org/10.1109/CHILECON60335.2023.10418676

Othmer HG, Dunbar SR, Alt W (1988) Models of dispersal in biological systems. *J Math Biol* 26:263–298. https://doi.org/10.1007/BF00277392

Pazy A (1983) *Semigroups of Linear Operators and Applications to Partial Differential Equations*. Springer, New York. https://doi.org/10.1007/978-1-4612-5561-1

Peres NA, Timmer LW, Adaskaveg JE, Correll JC (2020) Managing *Colletotrichum* on fruit crops: a "complex" challenge. *Plant Dis* 104:2301–2316. https://doi.org/10.1094/PDIS-11-19-2378-FE

Riquelme D, Aravena Z, Valdés-Gómez H, Latorre BA, Díaz GA, Zoffoli JP (2021) Characterization of *Botrytis cinerea* and *B. prunorum* from healthy floral structures and decayed 'Hayward' kiwifruit during post-harvest storage. *Plant Dis* 105(8):2129–2140. https://doi.org/10.1094/PDIS-04-20-0878-RE

Shen W, Xie X (2015) On principal spectrum points/principal eigenvalues of nonlocal dispersal operators and applications. *Discrete Contin Dyn Syst* 35:1665–1696. https://doi.org/10.3934/dcds.2015.35.1665

Tian X, Du Q (2013) Analysis and comparison of different approximations to nonlocal diffusion and linear peridynamic equations. *SIAM J Numer Anal* 51:3458–3482. https://doi.org/10.1137/13091631X

van den Driessche P, Watmough J (2002) Reproduction numbers and sub-threshold endemic equilibria for compartmental models. *Math Biosci* 180:29–48. https://doi.org/10.1016/S0025-5564(02)00108-6

Williamson B, Tudzynski B, Tudzynski P, van Kan JAL (2007) *Botrytis cinerea*: the cause of grey mould disease. *Mol Plant Pathol* 8:561–580. https://doi.org/10.1111/j.1364-3703.2007.00417.x